Retrieval of Cloud Condensation Nuclei Number Concentration Profiles from Lidar Extinction and Backscatter Data

Min Lv[1], Zhien Wang[2], Zhanqing Li[1,3]*, Tao Luo[4], Richard Ferrare[5], Dong Liu[4], Decheng Wu[4], Jietai Mao[6], Bingcheng Wan[7], Fang Zhang[1], Yuying Wang[1]

[1]State Key Laboratory of Earth Surface Processes and Resource Ecology and College of Global Change and Earth System Science, Beijing Normal University, Beijing, China,

[2] Department of Atmospheric Science, University of Wyoming, Laramie, Wyoming, USA,

[3]University of Maryland, College Park, Maryland, USA,

[4]Key Laboratory of Atmospheric Composition and Optical Radiation, Anhui Institute of Optics and Fine Mechanics, Chinese Academy of Sciences, Anhui, China,

[5] NASA Langley Research Center, Hampton, Virginia, USA

[6]School of Physics, Peking University, Beijing, China,

[7]State Key Laboratory of Atmospheric Boundary Layer Physics and Atmospheric Chemistry, Institute of Atmospheric Physics, Chinese Academy of Sciences, Beijing, China.

Corresponding author: Zhanqing Li, zhanqing@umd.edu

Key Points:

- An algorithm is proposed to retrieve vertical profiles of CCN from lidar measurements
- The potential of the algorithm is demonstrated with numerical simulations and observations
- CCN retrievals from lidar are in good agreement with in situ measurements

Abstract

The vertical distribution of aerosols and their capability of serving as cloud condensation nuclei (CCN) are important for improving our understanding of aerosol indirect effects. Although ground-based and airborne CCN measurements have been made, they are generally scarce, especially at cloud base where it is needed most. We have developed an algorithm for profiling CCN number concentrations using backscatter coefficients at 355, 532, and 1064 nm and extinction coefficients at 355 and 532 nm from multi-wavelength lidar systems. The algorithm considers three distinct types of aerosols (urban industrial, biomass burning, and dust) with bimodal size distributions. The algorithm uses look-up tables, which were developed based on the ranges of aerosol size distributions obtained from the Aerosol Robotic Network, to efficiently find optimal solutions. CCN number concentrations at five supersaturations (0.07–0.80%) are determined from the retrieved particle size distributions. Retrieval simulations were performed with different combinations of systematic and random errors in lidar-derived extinction and backscatter coefficients: systematic errors range from -20% to 20% and random errors are up to 15%, which fall within the typical error ranges for most current lidar systems. The potential of this algorithm to retrieve CCN concentrations is further evaluated through comparisons with surface-based CCN measurements with near surface lidar retrievals. This retrieval algorithm would be valuable for aerosol-cloud interaction studies for which virtually none has employed CCN at cloud base because of the lack of such measurements.

1. Introduction

Atmospheric aerosol particles affect climate indirectly by acting as cloud condensation nuclei (CCN) [*Carslaw et al*., 2010; *Paasonen et al*., 2013]. CCN are those aerosol particles on which cloud droplets form when the supersaturation in a cloud is high enough for the particles to grow by water condensation until they reach a critical radius, beyond which condensational growth continues spontaneously unless the supersaturation decreases rapidly [*Nenes et al*. 2001b; *Mamouri and Ansmann*, 2016]. Anthropogenic emissions of aerosol particles are a major source of CCN, which influence cloud microphysical and radiative properties, and consequently climate change [*Boucher et al*., 2013]. Therefore, an accurate knowledge of the spatial distribution of aerosols and their capability of serving as CCN is fundamental to understanding aerosol indirect effects. As emphasized by *Fan et al*. [2016], obtaining concurrent measurements of aerosol properties and cloud microphysical and dynamic properties over a range of temporal and spatial scales is critical to advance our understanding of aerosol-cloud interactions.

CCN can be measured in situ from the ground [*Feingold and Grund*, 1994; *Roberts and Nenes*, 2005] and from aircraft [*Rosenfeld et al.*, 2008; *Li et al.*, 2015a, b], or inferred from satellite observations [*Grandey and Stier*, 2010; *Gryspeerdt et al.*, 2014; *Shinozuka et al.*, 2015; *Rosenfeld et al.*, 2016]. Long-term monitoring of CCN properties at different observation sites has been chiefly made on the ground. Other than limited horizontal cover and many other issues [*Paramonov et al.*, 2013], near-surface CCN properties could be significantly different from CCN properties near the cloud base due to vertical aerosol inhomogeneities, especially air pollution under stable atmospheric boundary conditions. Except for *Rosenfeld et al.* [2016], satellite-based CCN estimations mainly use aerosol optical depth as a proxy for aerosol loading to take advantage of its global coverage. It is still challenging and highly uncertain [*Andreae*, 2009; *Liu and Li*, 2014] with many other limitations such as a lower temporal resolution, cloud contamination, and aerosol swelling in the moist environment near clouds [*Koren et al.*, 2007]. Airborne measurements can provide CCN measurements near cloud base, but are expensive to collect and are limited to a few field experiments [*Feingold et al*., 1998; *Li et al.*, 2015a, b]. The capability of routinely measuring new CCN at cloud base to study aerosol-cloud-precipitation interactions effectively is still lacking [*Burkart et al.*, 2011].

Vertically-resolved aerosol measurements offered by lidars provide the potential to measure CCN near cloud base. *Feingold et al.* [1998] developed an approach that used a combination of several remote sensing instruments, such as the Ka-band Doppler radar, the microwave radiometer, and the lidar, to derive the activation of CCN as a function of supersaturation level. However, this approach is based on the Junge power-law aerosol size distribution [*Junge*, 1952] that is only applicable for a clean troposphere and stratosphere. *Ghan and Collins* [2004] and *Ghan et al.* [2006] developed a technique to estimate CCN at cloud base based on the relationship between the aerosol extinction from lidar and CCN concentrations from near-surface measurements. However, their methods rely on the assumption that the aerosol composition and the shape of the aerosol size distribution at the surface are representative of the vertical column. Thus, their retrievals may have high uncertainties if the vertical profile of the shape of the aerosol size distribution differs markedly from that at the surface. In addition to their common use in profiling atmospheric temperature and humidity [*Wandinger*, 2005], multi-wavelength Raman lidars and High Spectral Resolution Lidars (HSRL) have been increasingly used in recent years to retrieve aerosol and CCN properties [*Müller et al.*, 1999; *Chemyakin et al.*, 2014; *Mamouri and Ansmann*, 2016]. This type of lidar allows for independent inferences of particle backscatter and extinction coefficients without the need for assuming any atmospheric parameters. Multi-wavelength Raman lidars can thus be used to quantify the main aerosol microphysical parameters and CCN properties with fewer a priori assumptions. The retrieval of aerosol microphysical properties is mainly based on the regularization algorithm [*Müller et al.*, 1999, 2000, 2014; *Veselovskii et al.*, 2002, 2004, 2013; *Chemyakin et al.*, 2014, 2016]. Most of these early studies focused on aerosol size distribution and total aerosol concentration retrievals, and used the regularization technique, which lead to higher sensitivities with a 1-sigma value of 61.4–95.2% for different aerosol types [*Pérez-Ramírez et al*., 2013]. This is because total aerosol concentration is very sensitive to aerosols with diameters smaller than 50 nm and lidar observations offer almost no constraint for them. To ourknowledge, limited attempts have been made to quantify CCN concentrations from multi-wavelength lidar measurements. *Feingold and Grund* [1994] explored the potential of using multi-wavelength lidar measurements, but they only performed a simulation by using the theoretical wavelengths of289, 532,1064, 2020 and 11150 nm that some wavelengths are not available in real measurements. From the simulation, they only provided some relationships between multi-wavelength backscatter coefficients with the median radius and did not quantify any aerosol or CCN parameter.

In this paper, we propose a retrieval approach to estimate CCN number concentrations from multi-wavelength lidar extinction and backscatter coefficients. The approach is implemented with look-up tables (LUTs) to provide stable and efficient retrievals. CCN number concentrations at five critical supersaturation ratios (S_cs, 0.07–0.80%) are determined from the retrieved aerosol size distributions. The retrieval accuracies are evaluated using simulated lidar extinction and backscatter coefficients with both random and systematic errors. Since CCN retrievals are less sensitive to uncertainties in very small particles (nucleation-mode particles), it leads to much smaller errors in the retrievals of CCN number concentration than those focusing on total aerosol number concentrations as was done by most early studies due to little information on fine-mode aerosols from available lidar measurements. In Section 2, the inversion methodology is described. In Section 3, we present the numerical simulations. In Section 4, a real case study is presented. Conclusions are given in Section 5.

2. Methodology

2.1 Aerosol size distributions

As demonstrated by *Baars et al*. [2016], aerosol types can be identified by combining their Ångstrom exponent, lidar ratio, and depolarization ratio from multi-wavelength HSRL or Raman-polarization lidar measurements [*Burton et al*., 2012; *Groß et al*., 2013]. Therefore, our study assumes known aerosol types for CCN retrievals for the sake of tackling other more challenging tasks in retrieving CCN profiles.

Initially, three common and distinct aerosol types are considered in this study: urban industrial aerosols (Type 1), biomass-burning aerosols (Type 2), and dust aerosols (Type 3). Although particle size distributions are not always bimodal in each measurement case, their size distributions can be treated as a combination of fine and coarse modes with lognormal distributions, as widely used in aerosol remote sensing studies [*Veselovskii et al.*, 2004; *Remer et al.*, 2005; *Schuster et al*., 2006]. Multi-wavelength HSRL or Raman lidar measurements provide feasible constraints on these size parameters:

$$\frac{dn(r)}{d\ln(r)} = \sum_{i=f,c} \frac{N_{ti}}{(2\pi)^{1/2}\ln\sigma_i} \exp\left[-\frac{\left(\ln r - \ln r_i^n\right)^2}{2\left(\ln\sigma_i\right)^2}\right], \quad (1)$$

where N_{ti} is the total particle number concentration of the i^{th} mode and r_i^n is the median radius for the aerosol size distribution with n representing the number concentration distribution. The index

133 $i = f, c$ refers to the fine mode and coarse mode, respectively. The term $\ln\sigma_i$ is the mode width of
134 the i^{th} mode. This general aerosol size distribution shape is adopted in this study to improve the
135 accuracy of the CCN retrieval. The sensitivity test regarding the response of CCN to the
136 assumption of bimodal size distributions is presented in Section 3.2.

137 Table 1 lists the typical ranges of the bimodal distribution parameters of the three types of
138 aerosols derived using measurements from sun and sky-scanning ground-based automated
139 radiometers at 12 selected Aerosol Robotic Network (AERONET) sites from 1993 to 2000
140 [*Dubovik et al.*, 2002; *Veselovskii et al.*, 2004]. Parameters representing the volume concentration
141 can be transformed to parameters for the number concentration through the following relationships
142 [*Horvath et al.*, 1990]:

143 $$r_i^n = r_i^v / \exp\left[3\left(\ln\sigma\right)^2\right], \quad (2)$$

144 $$V_{ti} = N_{ti}\frac{4}{3}\pi\left(r_i^n\right)^3 \exp\left[\frac{9}{2}\left(\ln\sigma\right)^2\right]. \quad (3)$$

145 As shown in Table 1 and Fig. 1, the main difference between the three aerosol types is the ratio
146 of the volume concentration of the fine mode to the volume concentration of the coarse mode.
147 Both urban industrial and biomass-burning aerosols have a predominance of fine-mode fractions
148 while the coarse mode dominates for dust aerosols.

149 **2.2 Inversion technique for aerosol size distribution parameters**

150 The first step in estimating CCN concentrations is to retrieve aerosol size distributions from
151 backscatter coefficients at 355, 532, and 1064 nm (β_{355}, β_{532}, β_{1064}) and extinction coefficients at
152 355 and 532 nm (α_{355}, α_{532}). These can be retrieved from multi-wavelength Raman lidar [*Ansmann*
153 *et al.*, 1992] or HSRL measurements [*Shipley et al*., 1983]. Aerosol type, which can be identified
154 from lidar measurements [*Burton et al*., 2012; *Groß et al*., 2013; *Baars et al*. 2016] provides the
155 mean complex refractive index (Table 1). Thus, retrieving six parameters (σ_f, N_{tf}, r_f, σ_c, N_{tc}, r_c) for
156 a bimodal size distribution from five known quantities (β_{355}, β_{532}, β_{1064}, α_{355}, α_{532}) is still an ill-
157 defined problem. Observations [*Dubovik et al*., 2002] indicate that the variation of the mode width
158 of the coarse mode ($ln\sigma_c$) is small for a given aerosol type and that the contribution of the coarse
159 mode to the total aerosol number concentration is relatively low. Therefore, we assume that $ln\sigma_c$

is a known quantity (Table 1). The retrieval errors from this assumption are examined in Section 3.3.

The retrieval algorithm searches for the best combination of five values (σ_f, N_{tf}, r_f, N_{tc}, r_c) to match inputs (β_{355}, β_{532}, β_{1064}, α_{355}, α_{532}) by minimizing the following function:

$$\rho^{sum} = \sum_i \left| \frac{g_i - g_i^{'}}{g_i} \right|, \left(i = 1,...,5\right), \tag{4}$$

where g_i represents input optical data (β_{355}, β_{532}, β_{1064}, α_{355}, α_{532}), and $g_i^{'}$ is optical data (β'_{355}, β'_{532}, β'_{1064}, α'_{355}, α'_{532}) calculated from Mie theory and size distribution parameters. Note that using the Mie theory for irregular-shaped dust aerosols can introduce potential systematic errors. It is a simplification for this simulation study. For future real-case applications, an improved optical database for dust aerosols will be developed following more advanced scattering calculations [*Nousiainen*, 2009; *Liu et al*., 2015]. Additionally, including depolarization measurements improves not only the ability to distinguish dust, but also overall dust retrievals [*Luo et al*., 2015].

To search for the optimal solution, look-up tables (LUTs) for each type of aerosol are constructed. To reduce the LUT size and its dimensions, each LUT consists of two parts. The size distribution shown in Eq. (1) can be rewritten as

$$\frac{dn(r)}{dln(r)} = \sum_{i=f,c} \left\{ \frac{1}{(2\pi)^{1/2} \ln\sigma_i} \exp\left[-\frac{\left(\ln r - \ln r_i^n\right)^2}{2\left(\ln\sigma_i\right)} \right] \bullet N_{ti} \right\} = \sum_{i=f,c} B_i \bullet N_{ti}, \tag{5}$$

where B_f and B_c refer to the data bank pre-computed with (σ_f, r_f, r) and (σ_c, r_c, r), respectively, where the intervals of σ_f, r_f, and r_c are fixed at 0.01, 0.002, and 0.01 μm, respectively, and where σ_c is assumed known and taken from Table 1. The range of r in the calculations is limited to 0.01–10 μm with a fixed bin size of 0.002 defined on a logarithmic-equidistant scale. These intervals are set as a compromise between accuracy and computation time.

Since the range of N_{tf} is usually large, the successive approximation method [*Kantorovitch*, 1939] is adopted:

Step 1: Calculate the corresponding optical data (β'_{355}, β'_{532}, β'_{1064}, α'_{355}, α'_{532}) from the data bank (B_f, B_c) and N_{tf}, N_{tc} (the step widths of N_{tf} and N_{tc}: 100 and 0.1 cm^{-3}, respectively). Search for an approximate solution based on the criterion in Eq. (4).

Step 2: Determine a smaller solution space of N_{tf} based on the approximate solution obtained in Step 1. Repeat the procedure in Step 1 except use a smaller step width of 10 cm^{-3} for N_{tf}. Search for the optimal solution of five parameters (σ_f, N_{tf}, r_f, N_{tc}, r_c).

2.3 CCN estimations

The ability of aerosols to act as CCN is mainly determined by three factors: aerosol particle size distribution, chemical composition, and mixing state. Several studies have suggested that it is controlled more by the aerosol size distribution than the chemical composition [*Junge and McLaren*, 1971; *Fitzgerald,* 1973; *Dusek et al*., 2006], however, for some specific areas and meteorological conditions, both factors are important [*Mamouri and Ansmann*, 2016]. If no suitable chemical composition data are available, using mean chemical composition information for each aerosol type denoted by a single value of κ is feasible to estimate the CCN number concentration. In reality, the uncertainty of using the mean value of κ to estimate the CCN number concentration varies with atmospheric conditions. Most studies show that the uncertainty is within 10% [*Jurányi et al*., 2010; *Deng et al*., 2011; *Wang et al*., 2018]. The hygroscopicity parameter κ describes the relationship between the particle dry diameter and CCN activity when compositional data are not available [*Petters and Kreidenweis*, 2007]. *Wang et al*., [2018] found that the sensitivity of the estimated CCN concentration to κ depends strongly on the variability of the shape of the aerosol size distribution. The sensitivity of CCN concentration to κ becomes weaker with increasing supersaturations, suggesting that chemical composition becomes less important in CCN concentration estimates at larger supersaturations. In addition, this study also suggested that using the mean value of $\kappa \approx 0.3$ can be a good proxy for urban industrial aerosol when estimating the CCN concentration. The κ is assumed to be 0.3 for Type 1 [*Liu et al.*, 2011], 0.1 for Type 2 [*Petters et al.*, 2009], and 0.03 for Type 3 [*Koehler et al.*, 2009] aerosols in the simulations. For actual measurements, the mixing state of aerosols and the precise values of κ can be determined with the aid of other instruments, such as the aerosol particle mass analyzer (APM), and the hygroscopic tandem differential mobility analyzer (HTDMA) [*Malloy et al*., 2009; *Zhang et al*., 2014; *Wang et al*., 2017]. For experiments without the HTDMA, a lidar can be used to roughly infer κ indirectly

by identifying aerosol types [*Baars et al*., 2016]. However, the determination of κ is beyond the scope of the current method.

We first determine the critical radius (r_c) of CCN activation at five critical S_cs for activation (0.07, 0.10, 0.20, 0.40, and 0.80%), which are often used for in CCN counters. The critical diameter D_c ($r_c = D_c / 2$) and S_c for activation (where $S_c = S - 1$) can be computed from the maximum of *κ*-Köhler curve as suggested by *Petters and Kreidenweis* [2007]:

$$S(D) = \frac{D^3 - D_d^3}{D^3 - D_d^3(1-\kappa)} \exp\left(\frac{4\sigma_{s/a} M_w}{RT\rho_w D}\right), \quad (6)$$

where S is the water saturation ratio, D is the droplet diameter, D_d is the dry diameter, $\sigma_{s/a} = 0.072$ J m^{-2}, M_w is the molecular weight of water, R is the universal gas constant, T is temperature and equal to 298.15 K, and ρ_w is the density of water. Equation (6) describes the relationship between the dry diameter and critical supersaturation for a selected hygroscopicity κ. Note that the Köhler theory used for dust CCN activation is based on the assumptions that activation is solely controlled by the amount of soluble salts in the dust aerosol and that it is not affected by water adsorption on the dust surface.

Figure 2 shows the relationship between critical dry diameter and critical supersaturation for each type of aerosol. Table 2 shows the critical radius (r_c) at five critical S_cs calculated using Eq. (6). The critical radius for each type of aerosol in Table 2 shows that CCN retrievals are mostly sensitive to particles with radii greater than 0.1 μm under normal atmospheric conditions, which indicates that neglecting nucleation-mode particles has a weaker impact on CCN determination than on the total aerosol number concentration retrievals.

It is noted that, to simplify the simulation, the impact of aerosol hygroscopic growth on the size distributions is not considered. However, in real atmosphere, the aerosol size distribution is affected by aerosol hygroscopic properties, especially when it is under high relative humidity conditions or near cloud base. In this case, the wet size distribution should be corrected to the dry size distribution by using the hygroscopic enhancement factor that is defined as

$$f(RH, r) = \frac{\xi(RH, r)}{\xi(RH_{ref}, r)} \quad (6)$$

where RH is the relative humidity, r is the dry radius, $\xi(RH,r)$ refers to a RH-dependent aerosol property at a certain r, the RH_{ref} is chosen as the lowest value of RH that represents the relative dry environment in a case. $f(RH,r)$ can be obtained from HTDMA or Raman lidar [*Veselovskii et al*., 2009; *Lv et al*. 2017]. For the determination of *f(RH)* from Raman lidar, it is based on the assumption of well-mixed atmospheric conditions that may be identified as having the constant profiles of potential temperature and water vapor simultaneously [*Granados-Muñoz et al*., 2015].

Finally, the CCN concentration can be calculated as

$$N_{ccn} = \int_{\ln r_c}^{\infty} \frac{dn(r)}{d\ln(r)}\, d\ln(r) \quad . \tag{7}$$

3. Numerical simulations

Due to the lack of reliable collocated CCN and lidar measurements, evaluating the algorithm is a challenging task. As the first step, the performance of the algorithm is evaluated using simulated observations with different error characteristics.

3.1 Inversion with error-free inputs

The first evaluation is performed under the assumption of error-free lidar measurements to understand the inversion stability. For each type of aerosol, 1000 different sets of bimodal size distributions are used to simulate lidar observations. The retrieval is repeated for each simulated observation. The retrieved parameters (σ_f, N_{tf}, r_f, N_{tc}, r_c) and assumed σ_c permit us to calculate the errors in retrieved CCN number concentration ($CCN_{retrieved}$) with respect to the initial inputs ($CCN_{initial}$), i.e., [($CCN_{retrieved}$ - $CCN_{initial}$)/ $CCN_{initial}$] * 100%. Apart from the mean values, we employ the standard deviations (SDs) of the CCN retrieval errors from the different bimodal size distribution datasets to gauge the range of the retrieved CCN errors as well. As shown in Table 3, initial CCN concentrations are well reproduced from the error-free inputs for each type of aerosol size distribution. The mean errors in retrieved CCN number concentrations are close to zero, but are not equal to zero due to striking an appropriate balance between the accuracy and processing time of the LUTs as mentioned in section 2.2. The higher the accuracy of the LUTs, the more time expensive are the calculations and the closer CCN errors approach zero. Moreover, the small SDs ($\leqslant$ ~0.3%) suggest that the variances of errors among the different aerosol size distributions are

also small. Overall, the retrieval results shown in Table 3 attest to the good accuracy and stability of the inversion algorithm for the three types of aerosols.

3.2 Sensitivity test of the assumed bimodal size distribution with error-free inputs

We test the sensitivity of the CCN retrieval to the assumption of the bimodal size distribution by exploring dust aerosol size distributions measured on 20 August 2006 during the NASA African Monsoon Multidisciplinary Analysis (NAMMA) campaign [Chen et al., 2011]. NAMMA particle size distributions were measured simultaneously by an Ultra-High Sensitivity Aerosol Spectrometer (UHSAS) for the 0.07–1 μm (geometric) diameter range [*Cai et al*., 2008] and a TSI model 3321 Aerodynamic Particle Sizer (APS) for the 0.7–5 μm (aerodynamic) diameter range [*Peters and Leith*, 2003]. Fifty full particle size distributions were constructed using the size conversion factor, which is defined as the ratio of aerodynamic diameter to geometric diameter. These full aerosol size distributions can be well represented by the tri-modal lognormal distributions reported by Chen et al. [2011]. For the purpose of this study, we produce corresponding bimodal fits representative of the observed size distributions. Figure 3 shows an example of the observed aerosol size distribution and the corresponding bimodal fits. It suggests that the observed dust aerosol size distributions can be qualitatively well represented by bimodal lognormal size distributions. To quantify the errors arising from the bimodal lognormal fits, we calculate CCN concentrations based on the bimodal-fits and compare them with those from the 50 observed size distributions. The κ of NAMMA dust aerosols is assumed to be 0.03 when calculating CCN concentrations at the five values of S_cs as described in Section 2.3. Table 4 shows the induced CCN errors from the bimodal fitting of 50 NAMMA aerosol size distributions. The absolute value of CCN retrieval errors is 4.2% with a SD of 3.3% when Sc = 0.20%. Although errors from the bimodal assumption are not negligible, the results suggest that bimodal lognormal aerosol size distributions are adequate for retrieving CCN concentrations.

3.3 Sensitivity test of the assumed $\ln\sigma_c$ with error-free inputs

As described in section 2.2, $\ln\sigma_c$ is assumed to be equal to 0.7, 0.7, and 0.65 in LUTs corresponding to the different aerosol types. However, the real $\ln\sigma_c$ may vary within a small range. A sensitivity test of the effects of this assumption on the retrieval results is performed. In this sensitivity test, the fixed values of $\ln\sigma_c$ are still used in the LUTs while the real values of $\ln\sigma_c$ in simulations is selected randomly from within the ranges 0.6–0.8, 0.7–0.8, and 0.6–0.7 for urban

297 industrial, biomass-burning, and desert dust aerosols, respectively [*Veselovskii et al.*, 2004]. One
298 thousand different sets of simulations are produced randomly with the other known parameters as
299 input. The same inversion procedure described in Section 3.1 is repeated to retrieve CCN
300 concentrations and to calculate the retrieval errors.

301 Table 5 shows CCN retrieval errors due to assuming a constant $\ln\sigma_c$. As expected, the
302 assumption of a constant $\ln\sigma_c$ introduces an additional CCN retrieval error. In general, CCN
303 retrieval errors at higher S_cs are larger than those at lower S_cs for all types of aerosols due to the
304 smaller critical radius, which makes CCN calculations more sensitive to fine-mode size
305 distribution shapes. The maximum absolute value of CCN errors is 3.4% when S_cs are 0.07% and
306 0.10%, and reaches 6.6% when the S_c is 0.80%. This suggests that assuming a constant $\ln\sigma_c$ is
307 reasonable although the errors resulting from the assumption are not negligible.

308 **3.4 Effect of systematic and random errors on the retrieval results**

309 **3.4.1 The impact of systematic errors**

310 Extinction and backscatter coefficients retrieved from multi-wavelength lidar measurements
311 contain systematic and random errors [*Ansmann et al.*, 1992]. Systematic errors can be induced by
312 experiment conditions, techniques, and our understanding of physical interactions. Systematic
313 errors ranging from -20% to 20% in intervals of 5% are considered for the extinction and
314 backscatter coefficients. In actual measurements, the Raman lidar or HSRL allows for the
315 independent calculation of extinction and backscatter coefficients by combining elastic and Raman
316 backscatter signals [*Ansmann et al*., 1992] and by taking advantage of the spectral distribution of
317 the lidar return signal to discriminate aerosol and molecular signals [*Shipley et al*., 1983]. The
318 systematic errors are thus assumed independent for individual lidar measurements in the
319 simulations. This error range is reasonable for most current lidar systems [*Pérez-Ramírez et al.*,
320 2013]. To better understand the impacts of individual input parameters, a systematic error is
321 applied to one input parameter at a time. We repeat the inversion to obtain a new set of aerosol
322 size distribution and $CCN_{retrieved}$ data. For each input parameter and error value, the procedure is
323 repeated with 200 sets of randomly-generated size distributions for each aerosol type. The CCN
324 percentage errors associated with systematic errors can be estimated by comparing retrieved and
325 initial CCN number concentrations as defined above.

326 Figure 4 shows how individual systematic errors impact retrievals. The slope of the curve
327 indicates the sensitivity of CCN errors to systematic errors in individual input parameters. A larger

slope implies a higher sensitivity of the CCN retrieval to the systematic error for a given input parameter. In general, retrievals are most sensitive to the errors in α_{355} and α_{532}, and are least sensitive to errors in β_{1064}, with β_{355} and β_{532} falling somewhere in the middle. It is also interesting to note that the results are less sensitive to β_{355}, β_{532}, and β_{1064} at $S_c s \leq 0.10\%$, but are more sensitive to them at $S_c s > 0.10\%$. These results suggest that reducing uncertainties in the extinction coefficients at 355 and 532 nm can effectively improve the CCN retrieval accuracy, while reducing uncertainties in the backscatter coefficients benefits CCN retrievals at higher $S_c s$. Figure 4 also suggests that the retrieval results are sensitive to the position of the activation radius (denoted by S_c). This effect is the most obvious for Type 2 aerosols. Retrieval uncertainties due to systematic errors in α_{532} are much lower at 0.10% than at other $S_c s$.

In addition, it is also clear that the impact of systematic errors in a given input parameter on CCN retrievals varies with S_c as illustrated by the different signs of the slopes (positive or negative). For example, for Type 3 aerosols, the slopes of α_{355} and β_{355} are negative and positive, respectively, with magnitudes of 0.07% and 0.10%. When S_c exceeds 0.20%, the slopes reverse. These differences most likely result from the reduced sensitivity of the retrieval to the coarse mode of the aerosol size distribution.

Furthermore, there are significant differences among the three types of aerosols. Type 3 aerosols have the largest absolute CCN errors and Type 1 aerosols have the smallest. These results are consistent with the weights of fine-mode aerosol particles for the three types of aerosols shown in Table 1. These results suggest that there are better constraints for fine-mode aerosols than for coarse-mode aerosols. Therefore, retrieval uncertainties for the coarse mode are higher which introduces larger CCN retrieval errors for aerosols with more weight in the coarse mode, such as Type 3 aerosols. Including additional lidar measurements at wavelengths longer than 1064 nm will reduce the retrieval errors for dust aerosols.

3.4.2 The impact of random errors

Thus far, only the influence of systematic errors on the inversion results has been considered which introduces mean biases in CCN retrievals. Random errors in observations produce random CCN retrieval errors. Random errors are generated by considering a Gaussian distribution centered at zero with a SD equal to 15% of a given input parameter. Random errors are applied to all input optical data simultaneously. For each type of aerosol, we repeat this simulation 5000 times. The statistical results are presented in Fig. 5 and Table 6.

At 0.07% and 0.10%, errors in retrieved CCN number concentrations also follow a Gaussian distribution for Type 1 and Type 2 aerosols. When S_c exceeds 0.20%, the Gaussian shape distributions disappear and the high frequencies shift to the edge of the distributions for all types of aerosols. Mean errors are relatively small and non-zero, which is mainly due to the different sensitivities of CCN retrievals to different optical data. These results also reveal that random errors in the input parameters may produce systematic errors in the CCN retrievals. At 0.07%, Type 3 aerosols show the largest shift (-20.0%) while Type 2 aerosols have the smallest shift (-1.0% at 0.10%). Among the three types of aerosols, the largest errors are found in Type 3 aerosols which contain larger particles. These results are consistent with the sensitivities to the systematic errors, which also have the largest errors for Type 3 aerosols. As discussed earlier, measurements considered in the current multi-wavelength lidar technique contain less information for larger particles. Including additional lidar measurements at longer wavelengths could improve Type 3 aerosol retrievals. The maximum values of relative errors decrease with increasing S_cs for all aerosol types (Table 6).

3.4.3 The impact of combined systematic and random errors

In reality, systematic and random errors co-exist in optical input parameters, so their concurrent effects need to be tested. However, for real cases, the input optical data (β_{355}, β_{532}, β_{1064}, α_{355}, α_{532}) might be obtained simultaneously from different lidar systems like the Raman lidar or the HSRL with over- or under-estimation of systematic errors appearing in different combinations. For well -designed lidar systems with reliable data processing procedure, it is a good to assume independent systematic errors. However, there do have cases, which can result in dependent systematic errors. For example, near range overlap corrections could introduce dependent systematic errors between 355nm extinction and backscattering and 532 nm extinction and backscattering. To simplify the simulation, we only evaluate the overall performance of the new method when systematic and random errors co-exist. The simulations are done by conducting additional simulations with both systematic and random errors occurring simultaneously. Systematic errors are randomly assigned a sign (over/underestimation) as was done by *Pérez-Ramírez et al.* [2013]. Systematic errors are difficult to reveal, whereas random errors can be revealed and reduced by repeating the measurements. Systematic errors of 0–20% with a step width of 5% are added to all optical input parameters (β_{355}, β_{532}, β_{1064}, α_{355}, α_{532}) concurrently. As for random errors, they are generated by

considering a Gaussian distribution centered at zero with a SD equal to 5% of a given input parameter. For each type of aerosol, simulations were performed 500 times. The CCN retrieval results are presented in Fig. 6 and Table 7.

For Type 3 aerosols, the largest mean CCN error is 25.8% at S_c = 0.07%. For Type 1 and Type 2 aerosols, mean CCN errors in all cases are less than 10.3%. These retrieved CCN errors are much smaller than those obtained in Section 3.4.1 when only the systematic error was considered at each wavelength independently. Adding errors for multiple optical input parameters simultaneously might compensate each other and improve the CCN retrievals. However, the SDs are larger with maximum values reaching 20.5%, 26.7%, and 53.1% for Type 1, Type 2, and Type 3 aerosols, respectively, due to the very large measurement errors created by the random combination of systematic and random errors.

4. A real case study

The evaluation of CCN retrievals depends critically on how well lidar and in situ measurements are matched, as matching errors can become overwhelming. Due to a lack of collocated measurements of the required quantities, we have not yet seen any evaluation done using real-case data. It is done here by comparing CCN derived from lidar measurements and measured by a Cloud Condensation Nuclei counter (CCNc) on the ground on 16 August 2015 at the U.S. Department of Energy's Atmospheric Radiation Measurement (ARM) Climate Research Facility Southern Great Plains (SGP) site.

Multi-wavelength lidar data were collected during the Combined HSRL and Raman lidar Measurement Study (CHARMS) intensive observation period (IOP) that occurred in August 2015 at the SGP site [*Ferrare et al*., 2017]. During the CHARMS IOP, aerosol backscatter profiles at 532 and 1064 nm, and aerosol extinct-ion profiles at 532 nm were acquired from the University of Wisconsin HSRL located at the SGP site. HSRL aerosol profiles, when combined with aerosol backscatter and extinction profiles at 355 nm collected by the SGP Raman lidar, provide a full set of three aerosol backscatter (355, 532, and 1064 nm) and two aerosol extinction (355 and 532 nm) profiles for CCN retrievals. CHARMS data were processed at temporal and vertical resolutions of 10 minutes and 0.06 kilometers, respectively. To avoid the impact of the overlap function on extinction and backscattering retrievals, the lower limit of the height range where CCN properties are retrieved from optical data is 0.6 km above ground level. We also set the upper limit of the retrieval height range as 3 km due to the low aerosol loading in higher layers. For comparison

purposes, in situ CCN concentrations under different supersaturation conditions (S_cs ranging from 0.1–0.75%) were measured on the ground by the CCNc at the same site.

Although the SGP site is located in a rural area surrounded by cattle pastures and agricultural fields, air masses transported from the south and southeast often arrive at this site in the summer [*Mahish and Collins*, 2017]. Based on an overview of aerosol-type-dependent properties from more than 10 years of lidar observations [*Baars et al*., 2016] and Fig. 7, we can infer that aerosols in this case are not dust but urban or biomass burning aerosols by virtue of the lidar ratio (Fig. 7a), the depolarization ratio (Fig. 7b) and the Ångström exponent (Fig. 7c). The aerosol depolarization ratio was less than 0.1 on this day, which indicates that using the Mie theory for CCN retrievals is reasonable although potential systematic errors introduced by irregular-shaped aerosols are not negligible. To further distinguish between these two aerosol types, 48-h back trajectories calculated using the Hybrid Single-Particle Lagrangian Integrated Trajectory model [*Draxler and Rolph*, 2003] and active fire spots from Moderate Resolution Imaging Spectroradiometer (MODIS) data [*Giglio et al*., 2016] on 15 August 2015 are also used. Fig. 8a and Fig. 8b show that aerosols on 16 August 2015 originated from fire activities in the southeast and northeast of the SGP site. Therefore, the aerosol loading in this case was greatly influenced by biomass-burning aerosols transported to the SGP site. Based on the analysis of a multi-year record of hygroscopic measurements made at the SGP site [*Mahish and Collins*, 2017], a simplified hygroscopicity parameter κ equal to 0.2 is chosen for CCN retrievals here. This value falls within the reasonable range of κ for biomass-burning aerosols [*Petters et al.*, 2009].

Total particle number concentrations (condensation nuclei, CN) retrievals from the lidar are shown in Fig. 9. Fig. 9a shows the temporal evolution of the vertical profile of aerosol extinction at 355 nm in the 0.6–3 km height ranging from 0000 universal coordinated time (UTC) to 2400 UTC on 16 August 2015. During that day, a distinct aerosol layer was observed near the ground with an extinction coefficient of up to 0.25 km^{-1}. From 1200–2400 UTC, the aerosol layer increased in altitude up to 2.2 km due to the enhancement of turbulent mixing in the atmosphere. Above that layer, several weak aerosol layers appeared and aerosols were distributed more uniformly with height. The CN number concentrations which is computed from the retrieved size distribution parameters are shown in Fig. 9b.

Based on an investigation of the spatio-temporal distributions of *RH* at SGP during that day, the maximum *RH* is lower than 70% at each height and lower than 60% at 0.6 km, which didn't

reach the deliquescence *RH* of biomass burning aerosols [*Lei et al*., 2014; *Kuang et al*., 2016]. Thus the aerosol size distributions used for estimating CCN number concentrations are little influenced by aerosol hygroscopic growth on that day. For a comparison with surface in-situ measurements, retrieved CCN number concentrations are calculated using Eq. (7) with time-dependent supersaturations set for the in situ CCNc. Figure 10 shows the spatio-temporal distributions of CCN number concentrations (Fig. 10a), the time series of lidar-retrieved and surface-measured CCN concentrations (Fig. 10b) and a scatterplot of surface-measured CCN concentrations as a function of lidar-retrieved CCN concentration (Fig. 10c) respectively. Lidar retrievals shown in Fig. 10b and Fig. 10c are within a height range of 0.6 km. Figure 10a shows that the retrieved CCN number concentrations are roughly constant with height in the boundary layer except for the CCN number concentrations around 15:00 (UTC) that is likely due to the atmospheric transportation. The time series shows that both instruments generally captured the temporal evolution of CCN concentration on that day at the SGP site (Fig. 10b). However, periods with substantially different CCN concentrations were also observed. For example, higher CCN concentrations at ground level than at 0.6 km in the evening and overnight (0000–1000 UTC) are seen, most likely due to the vertically inhomogeneous distribution of aerosols. Figure 10c shows that CCN concentrations derived from measurements made by both instruments were well correlated. The correlation coefficient is 0.57 and the regression slope is 1.06 with most points lying close to the 1:1 line. Other than the vertical inhomogeneity of the atmosphere, most of the remaining differences could be due to the different observation methods and the extinction and backscattering retrieval uncertainties from the two lidar systems. Although a detailed uncertainty analysis is still needed and will be done in a future study, this comparison demonstrates the potential of using multi-wavelength Raman lidar measurements to profile aerosol and CCN properties.

5. Conclusions

We have investigated the feasibility of retrieving CCN number concentrations using multi-wavelength HSRL and Raman lidar measurements. Three representative types of aerosols with bimodal size distributions retrieved from AERONET observations were considered, namely, urban industrial (Type 1), biomass burning (Type 2), and dust (Type 3). The aerosol types are assumed known and provide the mean complex refractive index. This leaves six size parameters to retrieve. To avoid the ill-posed inversion problem, the mode width of the coarse mode is assumed.

Sensitivity tests suggest that this assumption only introduces a small error in the retrieval results. The retrieval is implemented based on LUTs generated from Mie scattering calculations. A successive approximation method in two steps is utilized as a tradeoff between the accuracy and computation time of the inversion. Once the parameters of the aerosol size distribution are obtained through the LUT, CCN number concentrations can be estimated.

Numerical simulations were performed to evaluate the algorithm performance with and without errors in the extinction and backscatter coefficients. For error-free input, CCN concentrations for the three types of aerosols were well reproduced with good accuracy and stability. Simulations with systematic errors show that the uncertainties of extinction coefficients at 355 and 532 nm have a higher impact on the retrieval results, and that retrievals are more dependent on the uncertainties in backscatter coefficients at higher S_cs than at lower S_cs. There are significant differences in retrieval uncertainties among the three types of aerosols due to the different weights of fine- and coarse-mode aerosol particles among them. The differences can be explained by the weaker constraint of the algorithm for the coarse mode of aerosol particles than for the fine mode of particles. Tests where 15% random errors were considered were done next. CCN number concentrations had Gaussian distributions at lower S_cs (0.07%, 0.10%) for all types of aerosols except for Type 3. This distribution shape disappeared at higher S_cs. Simulations with both random and systematic errors, which represent more realistic cases, show that both errors together improved mean CCN retrievals because random and systematic errors often offset each other. Simulations showed that if the input optical data had a 15% systematic error and a 5% random error simultaneously, CCN number concentrations were retrieved with an accuracy of -3.3 ± 18.7% for urban industrial aerosols, -7.6 ± 15.3% for biomass burning aerosols, and -24.9 ± 48.3% for dust aerosols at S_c = 0.07%.

The focus of the numerical simulations is to explore the sensitivity of CCN retrievals to errors in the measurements of extinction and backscatter coefficients. The influences of aerosol hydration and dynamic mixing on the refractive index are not considered in the simulations. When processing observational data, the impact of relative humidity needs to be accounted for since the lidars retrieve the wet size distributions while the CCN calculations require the dry size distribution. From Raman lidar measurements, temperature and water vapor below clouds can be determined to provide the vertical profile of relative humidity [*Ferrare*, 2000; *Behrendt et al*., 2002; *Reichardt et al*., 2012]. Aerosol-type-dependent hygroscopic growth may thus be needed to estimate the dry

size distribution from the wet size distribution and *RH* for CCN calculations. Furthermore, relative humidity information can be used to adjust the mean reflective index for the LUT. The impacts of humidity and the non-spherical dust shape will be studied and implemented, if warranted, in future algorithm development.

The algorithm was applied to observational data from the ARM Climate Research Facility SGP site to illustrate the potential of the algorithm. For the first time, lidar-retrieved CCN concentrations were compared with simultaneous measurements from an in situ CCNc. Considering the vertical aerosol inhomogeneity between the surface and 0.6 km above ground level, CCN concentrations from in situ measurements and lidar retrievals agree well.

The study demonstrates the potential of using multi-wavelength Raman lidar measurements to profile aerosol and CCN properties. The height-dependent information of aerosols and CCN are important for investigating the aerosol indirect effect in climate models. To ensure retrieval accuracy, 355 and 532 nm extinction coefficients need to be reliably derived. It is also important to consider including measurements made at longer wavelengths to improve CCN retrievals for dust aerosols.

Acknowledgements

Data were obtained from the ARM Climate Research Facility, a U.S. Department of Energy Office of Science User Facility sponsored by the Office of Biological and Environmental Research. Special thanks are extended to principal investigators Richard Ferrare and Tyler Thorsen, who provided the CHARMS Combined Dataset over the ARM SGP site. The Raman lidar measurements were made possible by John Goldsmith (Sandia National Laboratories); the HSRL data were made possible by Ed Eloranta, Willem Marais, and Robert Holz (University of Wisconsin-Madison). The data can be downloaded from http://www.archive.arm.gov/. The author would like to thank the NAMMA science team for providing the aerosol size distributions data. This work was supported by the National Basic Research Program of China on Global Changes (2013CB955802, 2013CB955804) and the National Natural Science Foundation of the U.S. (AGS-1337599, AGS1534670). Three reviewers are gratefully acknowledged for their constructive comments which helped improve the manuscript considerably.

References

Andreae, M. O. (2009), Correlation between cloud condensation nuclei concentration and aerosol optical thickness in remote and polluted regions, *Atmos. Chem. Phys*., *9*(2), 543–556, doi:10.5194/acp-9-543-2009.

Ansmann, A., M. Riebesell, U. Wandinger, C. Weitkamp, E. Voss, W. Lahmann, and W. Michaelis (1992), Combined raman elastic-backscatter LIDAR for vertical profiling of moisture, aerosol extinction, backscatter, and LIDAR ratio, *Appl. Phys. B*, *55*(1), 18–28, doi:10.1007/BF00348608.

Baars, H., et al. (2016), An overview of the first decade of PollyNET: an emerging network of automated Raman-polarization lidars for continuous aerosol profiling, *Atmos. Chem. Phys*., *16*(8), 5111–5137, doi:10.5194/acp-16-5111-2016.

Behrendt, A., T. Nakamura, M. Onishi, R. Baumgart, and T. Tsuda (2002), Combined Raman lidar for the measurement of atmospheric temperature, water vapor, particle extinction coefficient, and particle backscatter coefficient, *Appl. Opt*., *41*(36), 7657–7666, doi:10.1364/AO.41.007657.

Boucher, O., D. Randall, P. Artaxo, C. Bretherton, G. Feingold, P. Forster, V.-M. Kerminen, Y. Kondo, H. Liao, and U. Lohmann (2013), Clouds and aerosols, in *Climate change 2013: The physical science basis. Contribution of working group I to the fifth assessment report of the intergovernmental panel on climate change*, edited by T. F. Stocker et al., pp. 571–657, Cambridge University Press.

Burkart, J., G. Steiner, G. Reischl, and R. Hitzenberger (2011), Long-term study of cloud condensation nuclei (CCN) activation of the atmospheric aerosol in Vienna, *Atmos. Environ.*, *45*(32), 5751–5759, doi:10.1016/j.atmosenv.2011.07.022.

Burton, S. P., R. A. Ferrare, C. A. Hostetler, J. W. Hair, R. R. Rogers, M. D. Obland, C. F. Butler, A. L. Cook, D. B. Harper, and K. D. Froyd (2012), Aerosol classification using airborne High Spectral Resolution Lidar measurements – methodology and examples, *Atmos. Meas. Tech.*, *5*(1), 73–98, doi:10.5194/amt-5-73-2012.

Cai, Y., D. C. Montague, W. Mooiweer-Bryan, and T. Deshler (2008), Performance characteristics of the ultra high sensitivity aerosol spectrometer for particles between 55 and 800 nm: Laboratory and field studies, *J. Aerosol Sci*., *39*, 759–769, doi:10.1016/j.jaerosci.2008.04.007.

570 Carslaw, K. S., O. Boucher, D. V. Spracklen, G. W. Mann, J. G. L. Rae, S. Woodward, and M.
571 Kulmala (2010), A review of natural aerosol interactions and feedbacks within the Earth system,
572 *Atmos. Chem. Phys., 10*(4), 1701–1737, doi:10.5194/acp-10-1701-2010.
573 Chemyakin, E., D. Müller, S. Burton, A. Kolgotin, C. Hostetler, and R. Ferrare (2014), Arrange
574 and average algorithm for the retrieval of aerosol parameters from multiwavelength high-
575 spectral-resolution lidar/Raman lidar data, *Appl. Opt.*, *53*(31), 7252–7266,
576 doi:10.1364/AO.53.007252.
577 Chemyakin, E., S. Burton, A. Kolgotin, D. Müller, C. Hostetler, and R. Ferrare (2016), Retrieval
578 of aerosol parameters from multiwavelength lidar: investigation of the underlying inverse
579 mathematical problem, *Appl. Opt.*, *55*(9), 2188–2202, doi:10.1364/AO.55.002188.
580 Chen, G., et al. (2011), Observations of Saharan dust microphysical and optical properties from
581 the Eastern Atlantic during NAMMA airborne field campaign, *Atmos. Chem. Phys*., *11*(2), 723–
582 740, doi:10.5194/acp-11-723-2011.
583 Deng, Z. Z., C. Zhao, N. Ma, P. Liu, L. Ran, W. Xu, J. Chen, Z. Liang, S. Liang, M. Huang (2011),
584 Size-resolved and bulk activation properties of aerosols in the North China Plain, *Atmos. Chem.*
585 *Phys*., *11*(8), 3835–3846, doi:10.5194/acp-11-3835-2011.
586 Draxler, R. R., and G. Rolph (2003), HYSPLIT (HYbrid Single-Particle Lagrangian Integrated
587 Trajectory) model access via NOAA ARL READY website (http://www.arl.noaa.
588 gov/ready/hysplit4. html). NOAA Air Resources Laboratory, Silver Spring, edited, Md.
589 Dubovik, O., B. Holben, T. F. Eck, A. Smirnov, Y. J. Kaufman, M. D. King, D. Tanré, and I.
590 Slutsker (2002), Variability of absorption and optical properties of key aerosol types observed
591 in worldwide locations, *J. Atmos. Sci.*, *59*(3), 590–608, doi:10.1175/1520-
592 0469(2002)059<0590:VOAAOP>2.0.CO;2.
593 Dusek, U., et al. (2006), Size matters more than chemistry for cloud-nucleating ability of aerosol
594 particles, *Science*, *312*(5778), 1375–1378, doi:10.1126/science.1125261.
595 Fan, J., Y. Wang, D. Rosenfeld, and X. Liu (2016), Review of Aerosol–Cloud Interactions:
596 Mechanisms, Significance, and Challenges, *J. Atmos. Sci.*, *73*(11), 4221–4252,
597 doi:10.1175/JAS-D-16-0037.1.
598 Ferrare, R. A. (2000), Raman lidar profiling of water vapor and aerosols over the ARM SGP site,
599 *Rep.*, Brookhaven National Lab., Upton, NY (US).

Ferrare, R. A. (2017), Characterizing the vertical distribution of aerosols above SGP using CHARMS data, ARM/ASR PI Meeting.

Feingold, G., and C. J. Grund (1994), Feasibility of using multiwavelength lidar measurements to measure cloud condensation nuclei, *J. Atmos. Ocean. Tech.*, *11*(6), 1543–1558, doi:10.1175/1520-0426(1994)011<1543:FOUMLM>2.0.CO;2.

Feingold, G., S. Yang, R. Hardesty, and W. Cotton (1998), Feasibility of retrieving cloud condensation nucleus properties from Doppler cloud radar, microwave radiometer, and lidar, *J. Atmos. Ocean. Tech.*, *15*(5), 1188–1195, doi:10.1175/1520-0426(1998)015<1188:FORCCN>2.0.CO;2.

Fitzgerald, J. W. (1973), Dependence of the supersaturation spectrum of CCN on aerosol size distribution and composition, *J. Atmos. Sci.*, *30*(4), 628–634, doi:10.1175/1520-0469(1973)030<0628:DOTSSO>2.0.CO;2.

Ghan, S. J., and D. R. Collins (2004), Use of in situ data to test a Raman lidar-based cloud condensation nuclei remote sensing method, *J. Atmos. Ocean. Tech.*, *21*(2), 387–394, doi:10.1175/1520-0426(2004)021<0387:UOISDT>2.0.CO;2.

Ghan, S. J., T. A. Rissman, R. Elleman, R. A. Ferrare, D. Turner, C. Flynn, J. Wang, J. Ogren, J. Hudson, and H. H. Jonsson (2006), Use of in situ cloud condensation nuclei, extinction, and aerosol size distribution measurements to test a method for retrieving cloud condensation nuclei profiles from surface measurements, *J. Geophys. Res. Atmos.*, *111*(D5), doi:10.1029/2004JD005752.

Giglio, L., W. Schroeder, and C. O. Justice (2016), The collection 6 MODIS active fire detection algorithm and fire products, *Rem. Sens. Environ.*, *178*, 31–41, doi: 10.1016/j.rse.2016.02.054.

Granados-Muñoz, M., F. Navas-Guzmán, J. Bravo-Aranda, J. Guerrero-Rascado, H. Lyamani, A. Valenzuela, G. Titos, J. Fernández-Gálvez, and L. Alados-Arboledas (2015), Hygroscopic growth of atmospheric aerosol particles based on active remote sensing and radiosounding measurements: selected cases in southeastern Spain, *Atmos. Meas. Tech.*, *8*(2), 705-718.

Grandey, B., and P. Stier (2010), A critical look at spatial scale choices in satellite-based aerosol indirect effect studies, *Atmos. Chem. Phys.*, *10*(23), 11459–11470, doi:10.5194/acp-10-11459-2010.

Groß, S., M. Esselborn, B. Weinzierl, M. Wirth, A. Fix, and A. Petzold (2013), Aerosol classification by airborne high spectral resolution lidar observations, *Atmos. Chem. Phys.*, *13*(5), 2487–2505, doi:10.5194/acp-13-2487-2013.

Gryspeerdt, E., P. Stier, and D. Partridge (2014), Satellite observations of cloud regime development: the role of aerosol processes, *Atmos. Chem. Phys.*, *14*(3), 1141–1158, doi:10.5194/acp-14-1141-2014.

Horvath, H., R. Gunter, and S. Wilkison (1990), Determination of the coarse mode of the atmospheric aerosol using data from a forward-scattering spectrometer probe, *Aerosol Sci. Tech.*, *12*(4), 964–980, doi:10.1080/02786829008959407.

Junge, C. (1952), Gesetzmäßigkeiten in der größenverteilung atmosphärischer aerosole über dem kontinent, *Berichte des deutschen Wetterdienstes*, *35*, 261–277.

Junge, C., and E. McLaren (1971), Relationship of cloud nuclei spectra to aerosol size distribution and composition, *J. Atmos. Sci.*, *28*(3), 382–390, doi:10.1175/1520-0469(1971)028<0382:ROCNST>2.0.CO;2.

Jurányi, Z., M. Gysel, E. Weingartner, P. F. DeCarlo, L. Kammermann, and U. Baltensperger (2010), Measured and modelled cloud condensation nuclei number concentration at the high alpine site Jungfraujoch, *Atmos. Chem. Phys*., *10*(16), 7891–7906, doi:10.5194/acp-10-7891-2010.

Kantorovitch, L. (1939), The method of successive approximation for functional equations, *Acta Mathematica*, *71*(1), 63–97, doi:10.1007/BF02547750.

Koehler, K., S. Kreidenweis, P. DeMott, M. Petters, A. Prenni, and C. Carrico (2009), Hygroscopicity and cloud droplet activation of mineral dust aerosol, *Geophys. Res. Lett.*, *36*(8), doi:10.1029/2009GL037348.

Koren, I., L. A. Remer, Y. J. Kaufman, Y. Rudich, and J. V. Martins (2007), On the twilight zone between clouds and aerosols, *Geophys. Res. Lett.*, *34*(8), doi:10.1029/2007GL029253.

Kuang, Y., C. S. Zhao, N. Ma, H. J. Liu, Y. X. Bian, J. C. Tao, and M. Hu (2016), Deliquescent phenomena of ambient aerosols on the North China Plain, *Geophys. Res. Lett.*, *43*, 8744–8750, doi:10.1002/2016GL070273.

Lei, T., A. Zuend, W. Wang, Y. Zhang, and M. Ge (2014), Hygroscopicity of organic compounds from biomass burning and their influence on the water uptake of mixed organic ammonium sulfate aerosols, *Atmos. Chem. Phys.*, *14*(20), 11165-11183.

660 Li, J., Y. Yin, P. Li, Z. Li, R. Li, M. Gribb, Z. Dong, F. Zhang, J. Li, G. Ren, L. Jin, and Y. Li
661 (2015a), Aircraft measurements of the vertical distribution and activation property of aerosol
662 particles over the Loess Plateau in China, *Atmos. Res.*, *155*, 73–86,
663 doi:10.1016/j.atmosres.2014.12.004.
664 Li, J., X. Liu, L. Yuan, Y. Yin, Z. Li, P. Li, G. Ren, L. Jin, R. Li, Z. Dong, Y. Li, and J. Yang
665 (2015b), Vertical distribution of aerosol optical properties based on aircraft measurements over
666 the Loess Plateau in China, *J. Environ. Sci.*, *34*, 44–56, doi:10.1016/j.jes.2015.01.021.
667 Liu, J., and Z. Li (2014), Estimation of cloud condensation nuclei concentration from aerosol
668 optical quantities: influential factors and uncertainties, *Atmos. Chem. Phys.*, *14*(1), 471–483,
669 doi:10.5194/acp-14-471-2014.
670 Liu, J., P. Yang, and K. Muinonen (2015), Dust-aerosol optical modeling with Gaussian spheres:
671 Combined invariant-imbedding T-matrix and geometric-optics approach, *J. Quant. Spectrosc.*
672 *Radiat. Transf.*, *161*, 136–144, doi:10.1016/j.jqsrt.2015.04.003.
673 Liu, P., C. Zhao, T. Göbel, E. Hallbauer, A. Nowak, L. Ran, W. Xu, Z. Deng, N. Ma, and K.
674 Mildenberger (2011), Hygroscopic properties of aerosol particles at high relative humidity and
675 their diurnal variations in the North China Plain, *Atmos. Chem. Phys.*, *11*(7), 3479–3494,
676 doi:10.5194/acp-11-3479-2011.
677 Luo, T., Z. Wang, R. A. Ferrare, C. A. Hostetler, R. Yuan, and D. Zhang (2015), Vertically
678 resolved separation of dust and other aerosol types by a new lidar depolarization method, *Opt.*
679 *Express, 23*(11), 14095-14107, doi:10.1364/OE.23.014095.
680 Lv, M., D. Liu, Z. Li, J. Mao, Y. Sun, Z. Wang,Y. Wang and C. Xie (2017), Hygroscopic growth
681 of atmospheric aerosol particles based on lidar, radiosonde, and in situ measurements: case
682 studies from the Xinzhou field campaign, *J. Quan. Spectrosc. Ra.*, *188*, 60-70,
683 doi:10.1016/j.jqsrt.2015.12.029.
684 Mahish, M., and D. Collins (2017), Analysis of a multi-year record of size-resolved hygroscopicity
685 measurements from a rural site in the US, *Aerosol Air Qual. Res.*, *17*, 1489–1500,
686 doi:10.4209/aaqr.2016.10.0443.
687 Malloy, Q. G., S. Nakao, L. Qi, R. Austin, C. Stothers, H. Hagino, and D. R. Cocker III (2009),
688 Real-time aerosol density determination utilizing a modified scanning mobility particle sizer—
689 aerosol particle mass analyzer system, *Aerosol Sci. Tech.*, *43*(7), 673–678, doi:
690 10.1080/02786820902832960.

691 Mamouri, R.-E., and A. Ansmann (2016), Potential of polarization lidar to provide profiles of
692 CCN-and INP-relevant aerosol parameters, *Atmos. Chem. Phys.*, *16*(9), 5905–5931, doi:
693 10.5194/acp-16-5905-2016.
694 Müller, D., U. Wandinger, and A. Ansmann (1999), Microphysical particle parameters from
695 extinction and backscatter lidar data by inversion with regularization: theory, *Appl. Opt.*, *38*(12),
696 2346–2357, doi:10.1364/AO.38.002346.
697 Müller, D., F. Wagner, U. Wandinger, A. Ansmann, M. Wendisch, D. Althausen, and W. von
698 Hoyningen-Huene (2000), Microphysical particle parameters from extinction and backscatter
699 lidar data by inversion with regularization: experiment, *Appl. Opt.*, *39*(12), 1879–1892,
700 doi:10.1364/AO.39.001879.
701 Müller, D., C. A. Hostetler, R. A. Ferrare, S. P. Burton, E. Chemyakin, A. Kolgotin, J. W. Hair,
702 A. L. Cook, D. B. Harper, R. R. Rogers, R. W. Hare, C. S. Cleckner, M. D. Obland, J. Tomlinson,
703 L. K. Berg, B. Schmid (2014), Airborne Multiwavelength High Spectral Resolution Lidar
704 (HSRL-2) observations during TCAP 2012: vertical profiles of optical and microphysical
705 properties of a smoke/urban haze plume over the northeastern coast of the US, *Atmos. Meas.*
706 *Tech.*, *7*(10), 3487–3496, doi:10.5194/amt-7-3487-2014.
707 Nenes, A., P. Y. Chuang, R. C. Flagan, and J. H. Seinfeld (2001), A theoretical analysis of cloud
708 condensation nucleus (CCN) instruments, *J. Geophys. Res. Atmos.*, *106*(D4), 3449–3474, doi:
709 10.1029/2000JD900614.
710 Nousiainen, T. (2009), Optical modeling of mineral dust particles: A review, *J. Quant. Spectrosc.*
711 *Radiat. Transf.*, *110*(14), 1261–1279, doi:10.1016/j.jqsrt.2009.03.002.
712 Paasonen, P., et al. (2013), Warming-induced increase in aerosol number concentration likely to
713 moderate climate change, *Nature Geosci, 6*(6), 438–442, doi:10.1038/ngeo1800.
714 Paramonov, M., P. P. Aalto, A. Asmi, N. Prisle, V. M. Kerminen, M. Kulmala, and T. Petäjä
715 (2013), The analysis of size-segregated cloud condensation nuclei counter (CCNC) data and its
716 implications for cloud droplet activation, *Atmos. Chem. Phys.*, *13*(20), 10285–10301,
717 doi:10.5194/acp-13-10285-2013.
718 Pérez-Ramírez, D., D. Whiteman, I. Veselovskii, A. Kolgotin, M. Korenskiy, and L. Alados-
719 Arboledas (2013), Effects of systematic and random errors on the retrieval of particle
720 microphysical properties from multiwavelength lidar measurements using inversion with
721 regularization, *Atmos. Meas. Tech*., *6*, 3039–3054, doi:10.5194/amt-6-3039-2013.

722 Peters, T. M., and D. Leith (2003), Concentration measurement and counting efficiency of the
723 aerodynamic particle sizer 3321, *J. Atmos. Sci.*, *34*(5), 627–634, doi:10.1016/S0021-
724 8502(03)00030-2.
725 Petters, M. D., and S. M. Kreidenweis (2007), A single parameter representation of hygroscopic
726 growth and cloud condensation nucleus activity, *Atmos. Chem. Phys.*, *7*(8), 1961–1971,
727 doi:10.5194/acp-7-1961-2007.
728 Petters, M. D., C. M. Carrico, S. M. Kreidenweis, A. J. Prenni, P. J. DeMott, J. L. Collett, and H.
729 Moosmueller (2009), Cloud condensation nucleation activity of biomass burning aerosol, *J.*
730 *Geophys. Res. Atmos.*, *114*(D22), doi:10.1029/2009JD012353.
731 Reichardt, J., U. Wandinger, V. Klein, I. Mattis, B. Hilber, and R. Begbie (2012), RAMSES:
732 German Meteorological Service autonomous Raman lidar for water vapor, temperature, aerosol,
733 and cloud measurements, *Appl. Opt*., *51*(34), 8111–8131, doi:10.1364/AO.51.008111.
734 Remer, L. A., Y. J. Kaufman, D. Tanré, S. Mattoo, D. A. Chu, J. V. Martins, R. R. Li, C. Ichoku,
735 R. C. Levy, R. G. Kleidman, T. F. Eck, E. Vermote, and B. N. Holben (2005), The MODIS
736 aerosol algorithm, products, and validation, *J. Atmos. Sci.*, *62*(4), 947–973,
737 doi:10.1175/JAS3385.1.
738 Roberts, G. C., and A. A. Nenes (2005), Continuous-flow streamwise thermal-gradient CCN
739 chamber for atmospheric measurements, *Aerosol Sci. Tech*., *39*(3), 206–221, doi:
740 10.1080/027868290913988.
741 Rosenfeld, D., W. L. Woodley, A. Lerner, G. Kelman, and D. T. Lindsey (2008), Satellite detection
742 of severe convective storms by their retrieved vertical profiles of cloud particle effective radius
743 and thermodynamic phase, *J. Geophys. Res. Atmos.*, *113*(D4), doi:10.1029/2007JD008600.
744 Rosenfeld, D., et al. (2016), Satellite retrieval of cloud condensation nuclei concentrations by using
745 clouds as CCN chambers, *Proc. Natl. Acad. Sci. U. S. A.*, *113*(21), 5828–5834,
746 doi:10.1073/pnas.1514044113.
747 Schuster, G. L., O. Dubovik, and B. N. Holben (2006), Angstrom exponent and bimodal aerosol
748 size distributions, *J. Geophys. Res. Atmos.*, *111*(D7), doi:10.1029/2005JD006328.
749 Shinozuka, Y., A. D. Clarke, A. Nenes, A. Jefferson, R. Wood, C. S. McNaughton, J. Ström, P.
750 Tunved, J. Redemann, K. L. Thornhill, R. H. Moore, T. L. Lathem, J. J. Lin and Y. J. Yoon
751 (2015), The relationship between cloud condensation nuclei (CCN) concentration and light
752 extinction of dried particles: indications of underlying aerosol processes and implications for

753 satellite-based CCN estimates, *Atmos. Chem. Phys.*, *15*(13), 7585–7604, doi:10.5194/acp-15-
754 7585-2015.
755 Shipley, S. T., D. Tracy, E. W. Eloranta, J. T. Trauger, J. Sroga, F. Roesler, and J. A. Weinman
756 (1983), High spectral resolution lidar to measure optical scattering properties of atmospheric
757 aerosols. 1: Theory and instrumentation, *Appl. Opt.*, *22*(23), 3716–3724.
758 Veselovskii, I., A. Kolgotin, V. Griaznov, D. Müller, U. Wandinger, and D. N. Whiteman (2002),
759 Inversion with regularization for the retrieval of tropospheric aerosol parameters from
760 multiwavelength lidar sounding, *Appl. Opt.*, *41*(18), 3685–3699, doi:10.1364/AO.41.003685.
761 Veselovskii, I., A. Kolgotin, V. Griaznov, D. Müller, K. Franke, and D. N. Whiteman (2004),
762 Inversion of multiwavelength Raman lidar data for retrieval of bimodal aerosol size distribution,
763 *Appl. Opt.*, *43*(5), 1180–1195, doi:10.1364/AO.43.001180.
764 Veselovskii, I., D. Whiteman, A. Kolgotin, E. Andrews, and M. Korenskii (2009), Demonstration
765 of aerosol property profiling by multiwavelength lidar under varying relative humidity
766 conditions, *J. Atmos. Ocean. Tech.*, *26*(8), 1543-1557.
767 Veselovskii, I., D. Whiteman, M. Korenskiy, A. Kolgotin, O. Dubovik, and D. Pérez-Ramírez
768 (2013), Retrieval of height-temporal distributions of particle parameters from multiwavelength
769 lidar measurements using linear estimation technique and comparison results with AERONET,
770 *Atmos. Meas. Tech.*, *6*, 2671–2682, doi:10.5194/amt-6-2671-2013.
771 Wandinger, U. (2005), Raman lidar techniques for the observation of atmospheric aerosols,
772 temperature, and humidity, paper presented at 13th International School on Quantum
773 Electronics: Laser Physics and Applications, International Society for Optics and Photonics.
774 Wang, Y., F. Zhang, Z. Li, H. Tan, H. Xu, J. Ren, J. Zhao, W. Du, and Y. Sun (2017), Enhanced
775 hydrophobicity and volatility of submicron aerosols under severe emission control conditions
776 in Beijing, *Atmos. Chem. Phys., 17*(8), 5239–5251, doi:10.5194/acp-17-5239-2017.
777 Wang, Y., Z. Li, Y. Zhang, W. Du, F. Zhang, H. Tan, H. Xu, X. Jin, X. Fan, Z. Dong, Q. Wang,
778 Y. Sun (2018), Characterization of aerosol hygroscopicity, mixing state, and CCN activity at a
779 suburban site in the central North China Plain, *Atmos. Chem. Phys. Discuss.*, 1 – 34.
780 Zhang, F., Y. Li, Z. Li, L. Sun, R. Li, C. Zhao, P. Wang, Y. Sun, X. Liu, J. Li, P. Li, G. Ren, and
781 T. Fan (2014), Aerosol hygroscopicity and cloud condensation nuclei activity during the
782 AC3Exp campaign: implications for cloud condensation nuclei parameterization, *Atmos. Chem.*
783 *Phys.*, *14*(24), 13423–13437, doi:10.5194/acp-14-13423-2014.

Figures

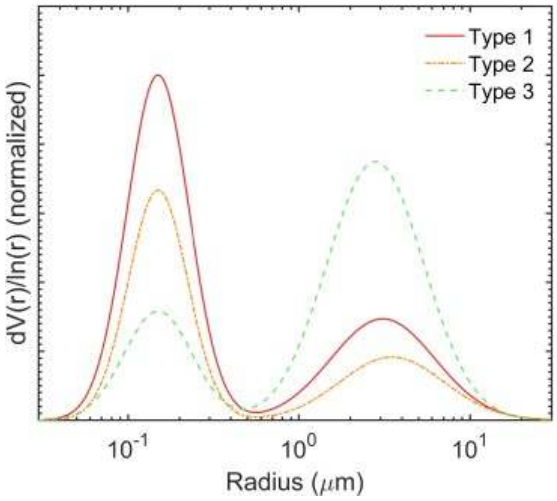

Figure 1. Normalized size distributions representing the three types of aerosols considered in this study. Types 1–3 represent urban industrial, biomass burning, and dust aerosols, respectively.

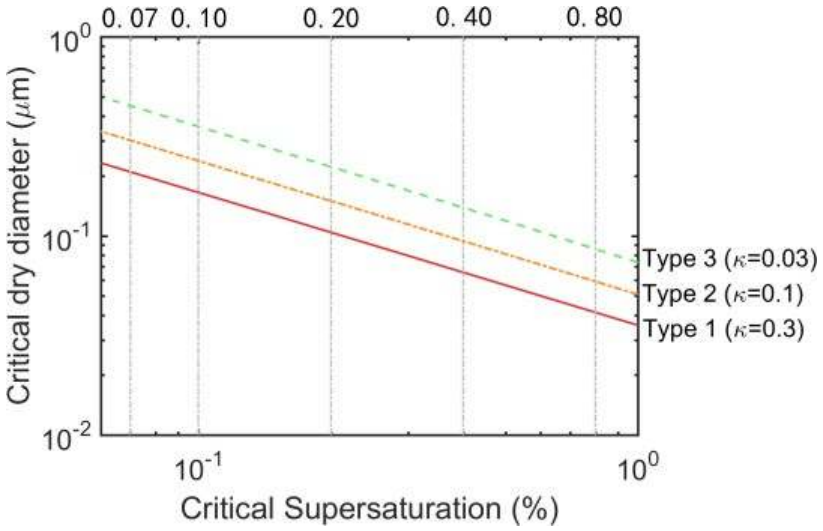

Figure 2. The relationship between particle critical dry diameter and critical supersaturation ratio for Type 1 (κ = 0.3), Type 2 (κ = 0.1), and Type 3 (κ = 0.01) aerosols. The parameter κ is the hygroscopicity parameter. Gray dashed lines denote the five critical S_cs for activation (0.07, 0.10, 0.20, 0.40, and 0.80%).

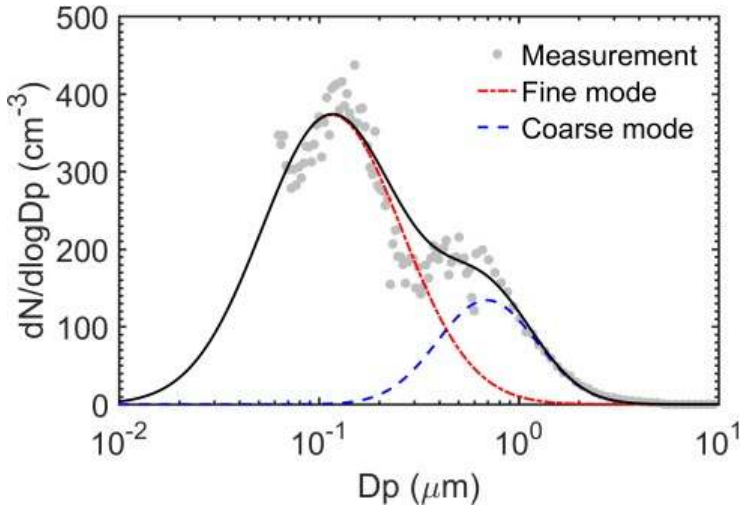

Figure 3. Observed particle number size distribution measured on 20 August 2006 during the NAMMA field campaign. Particle size is represented by the geometric diameter. Solid dots denote integrated UHSAS and APS measurements. Curves are bimodal lognormal fits for the size distributions of the fine mode (red dash-dotted line), the coarse mode (blue dashed line) and the full mode (black solid line).

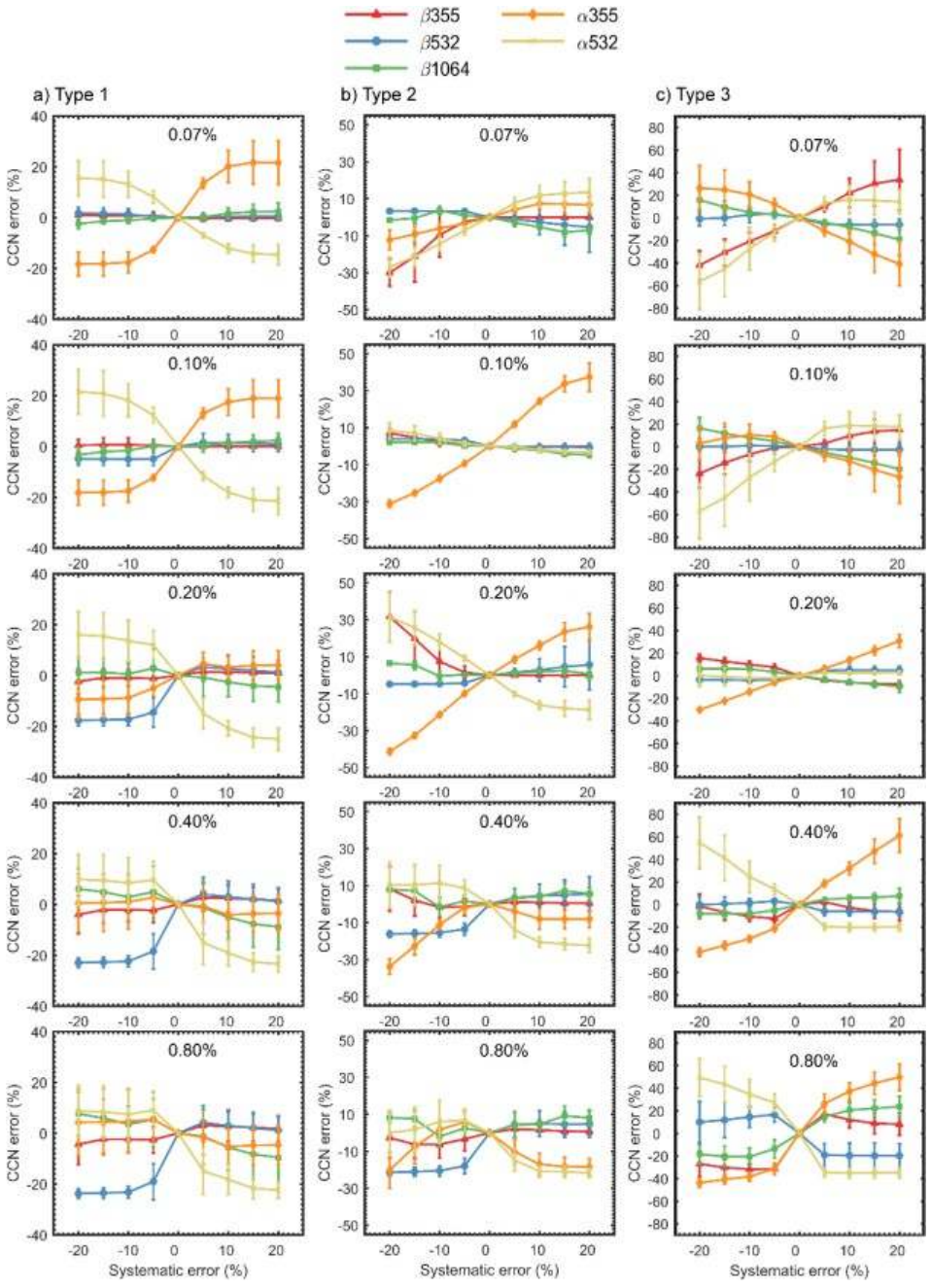

801

802 **Figure 4.** Errors in retrieved CCN number concentrations at different supersaturation ratios
803 (0.07%, 0.10%, 0.20%, 0.40%, and 0.80%) as a function of systematic errors in the input optical
804 data. Error bars denote the standard deviations for (a) Type 1, (b) Type 2, and (c) Type 3 aerosols.

805

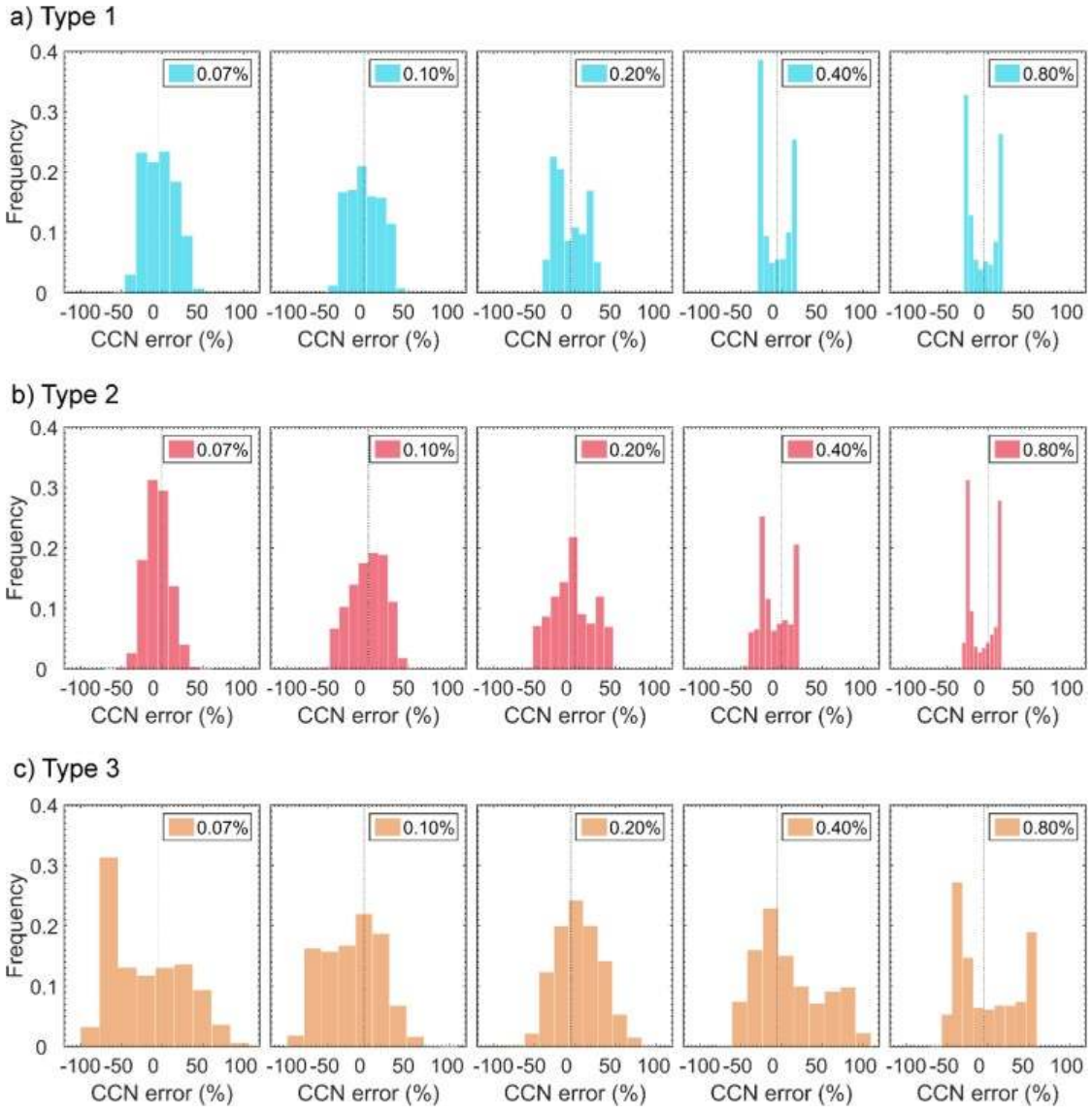

Figure 5. Frequency distributions of CCN errors for (a) Type 1, (b) Type 2, and (c) Type 3 aerosols at different supersaturation ratios (0.07%, 0.10%, 0.20%, 0.40%, and 0.80%) and with 15% random errors for all input optical data.

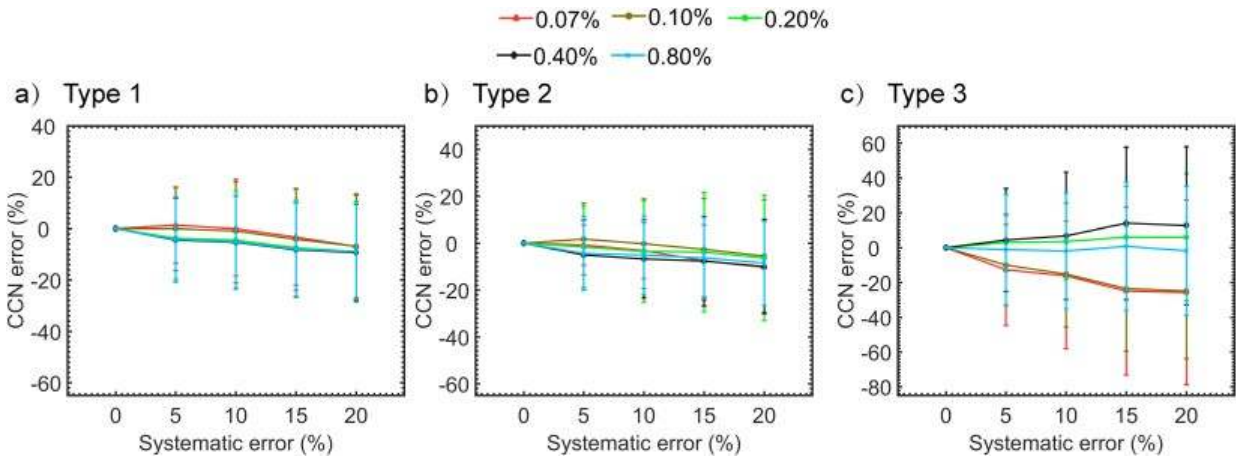

Figure 6. Errors in retrieved CCN number concentrations at different supersaturation ratios (0.07%, 0.10%, 0.20%, 0.40%, and 0.80%) that arise from accounting for both systematic and random errors for (a) Type 1, (b) Type 2, and (3) Type 3 aerosols. Error bars denote the standard deviations.

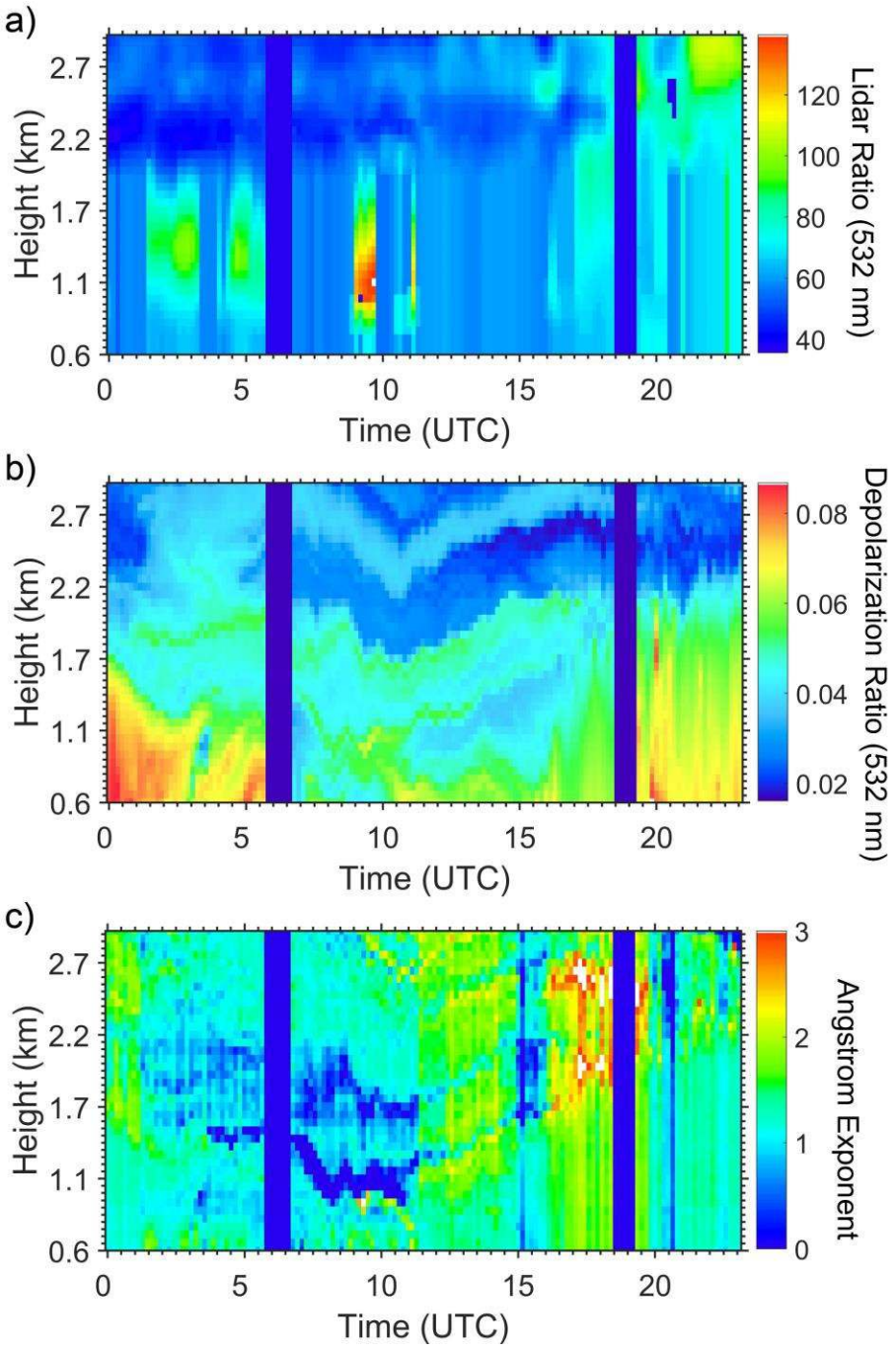

816

817 **Figure 7**. Spatio-temporal distributions of (a) the lidar ratio at 532 nm, and (b) the aerosol
818 depolarization ratio at 532 nm calculated from the Raman nitrogen signal, and (c) the Ångström
819 exponent retrieved from lidar measurements on 16 August 2015 at the SGP site. The heights are
820 kilometers above ground level.

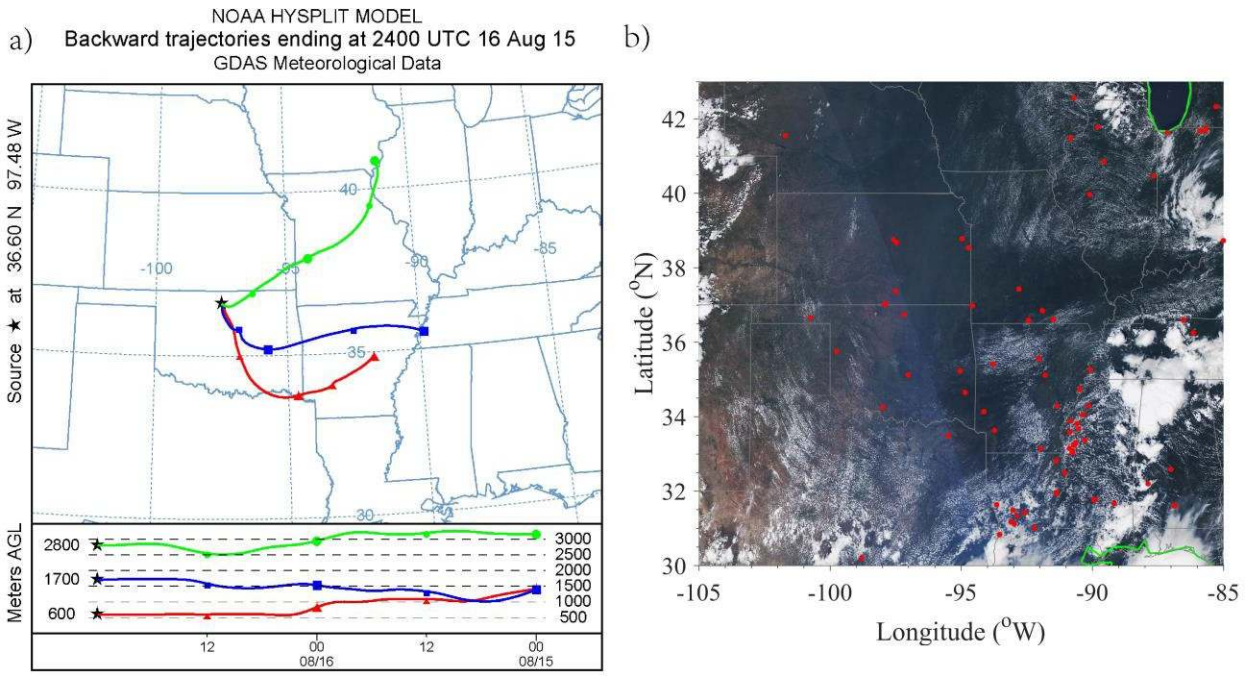

821

822 **Figure 8.** (a) 48-h back trajectories ending at 2400 UTC 16 August 2015 at the SGP site within
823 the 600–2800 m layer, (b) MODIS true RGB image along with fire spots (red dots) from Aqua and
824 Terra on 15 August 2015. The heights are meters above ground level.

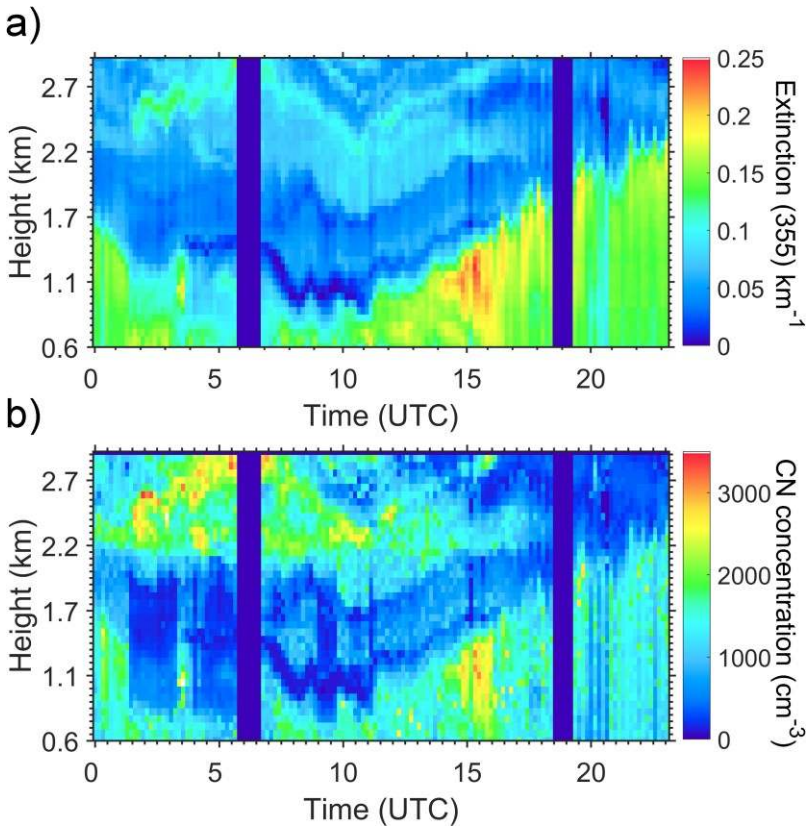

Figure 9. Spatio-temporal distributions of (a) aerosol extinction at 355 nm and (b) CN concentration retrieved from lidar measurements made on 16 August 2015 at the SGP site. The heights are kilometers above ground level.

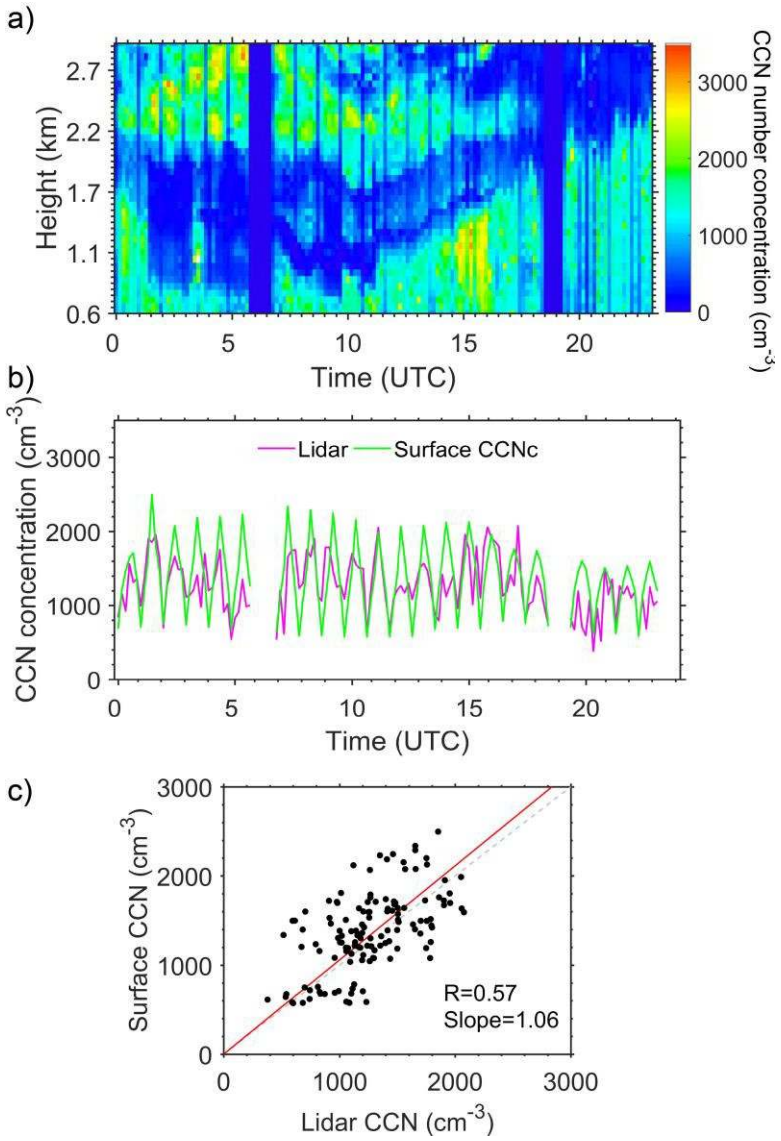

829

830 **Figure 10.** (a) Spatio-temporal distributions of retrieved CCN number concentrations. (b) Time
831 series of CCN concentration measured by the lidar (at 0.6 km, magenta line) and the surface CCNc
832 (green line). (c) Surface CCN concentration as a function of lidar CCN concentration (black dots)
833 on 16 August 2015 at the SGP site. The correlation coefficient (R) and the slope of the linear best-
834 fit line (red line) are given in the lower right corner of (c). The 1:1 line is also shown (grey dashed
835 line).

836

Tables

Table 1. Typical parameter ranges for the three aerosol bimodal distributions. V_{tf} / V_{tc} is the ratio of the volume concentration of the fine mode to the coarse mode. m_R and m_I represent the mean values of real and imaginary parts of the complex refractive index [*Dubovik et al.*, 2002; *Veselovskii et al.*, 2004].

Aerosol Parameter	Urban Industrial	Biomass Burning	Dust
r_f^n (μm)	0.075–0.095	0.072–0.082	0.062–0.082
r_c^n (μm)	0.60–0.71	0.75–0.80	0.59–0.64
ln σ_f	0.38–0.46	0.4–0.47	0.4–0.53
ln σ_c	0.70	0.70	0.65
V_{tf}/ V_{tc}	0.8–2.0	1.3–2.5	0.1–0.5
m_R, m_I	1.45, 0.01	1.5, 0.015	1.55, 0.002

Table 2. Critical radius at five critical supersaturation ratios for each type of aerosol.

	Critical Radius (r_c, μm)				
	0.07%	0.10%	0.20%	0.40%	0.80%
Type 1 (κ = 0.3)	0.105	0.083	0.052	0.033	0.021
Type 2 (κ = 0.1)	0.151	0.119	0.075	0.047	0.029
Type 3 (κ = 0.03)	0.224	0.177	0.111	0.069	0.043

Table 3. CCN errors at different S_cs (0.07%, 0.10%, 0.20%, 0.40%, and 0.80%) retrieved from error-free inputs for the three aerosol types.

		CCN Error (%)				
		0.07%	0.10%	0.20%	0.40%	0.80%
Mean ± SD (%)	Type 1	-0.01 ± 0.24	-0.01 ± 0.24	-0.01 ± 0.24	-0.01 ± 0.24	-0.01 ± 0.24
	Type 2	-0.01 ± 0.18	-0.01 ± 0.18	-0.01 ± 0.18	-0.01 ± 0.18	-0.01 ± 0.18
	Type 3	-0.00 ± 0.21	-0.00 ± 0.25	-0.00 ± 0.27	-0.00 ± 0.28	0.00 ± 0.28

Table 4. Sensitivity of CCN retrievals to the bimodal fits at different supersaturation ratios (0.07%, 0.10%, 0.20%, 0.40%, and 0.80%) from the 50 NAMMA aerosol size distributions. The CCN error is calculated as an absolute value.

	CCN Error (%)				
	0.07%	0.10%	0.20%	0.40%	0.80%
Mean ± SD (%)	3.9 ± 2.8	3.1± 2.9	4.2 ± 3.3	2.2 ± 1.8	1.9 ± 1.6

Table 5. Effects of the assumed $\ln\sigma_c$ on the retrieved CCN errors at different supersaturation ratios (0.07%, 0.10%, 0.20%, 0.40%, and 0.80%) for the three aerosol types. Error-free inputs were used.

		CCN Error (%)				
		0.07%	0.10%	0.20%	0.40%	0.80%
Mean ± SD (%)	Type 1	0.01 ± 0.7	-0.03 ± 1.2	-0.03 ± 3.8	0.02 ± 5.2	0.04 ± 5.5
	Type 2	0.8 ± 1.6	0.6 ± 1.0	-0.2 ± 1.2	-1.0 ± 3.0	-1.3 ± 3.9
	Type 3	-0.05 ± 2.7	0. 07 ± 3.3	0.3 ± 1.2	-0.2 ± 2.4	-0.8 ± 5.8

Table 6. Range, mean, and standard deviations of retrieved CCN number concentration errors at different supersaturation ratios (0.07%, 0.10%, 0.20%, 0.40%, and 0.80%). Input optical data included 15% random errors.

		0.07%	0.10%	0.20%	0.40%	0.80%
Type 1	Range (%)	[-53.4, 47.2]	[-49.4, 44.1]	[-37.9, 26.8]	[-30.0, 19.1]	[-27.5, 18.2]
	Mean ± SD (%)	-2.5 ± 18.7	-3.6 ±20.3	-7.0 ± 19.0	-7.6 ± 18.2	-7.3 ± 18.2
Type 2	Range (%)	[-61.7, 50.4]	[-53.0, 51.6]	[-55.1, 44.7]	[-43.8, 21.9]	[-31.2, 16.9]
	Mean ± SD (%)	-5.4 ± 14.6	-1.0 ± 21.4	-3.3 ± 24.9	-7.7± 18.9	-6.5 ± 17.5
Type 3	Range (%)	[-82.7, 122.6]	[-92.0, 103.4]	[-79.4, 98.1]	[-75.4, 103.5]	[-64, 57.7]
	Mean ± SD (%)	-20.0 ± 46.1	-19.4 ± 34.1	4.4 ± 27.5	10.2 ± 41.4	-0.8 ± 36.2

862 **Table 7.** Mean and standard deviations of CCN retrieval errors at different supersaturation ratios
863 (0.07%, 0.10%, 0.20%, 0.40%, and 0.80%) with both systematic and random errors included.

		Systematic error (%)	0.07%	0.10%	0.20%	0.40%	0.80%
Type 1	Mean ± SD (%)	5	1.3 ± 14.7	-0.1 ± 16.3	-3.7 ± 15.9	-4.5 ± 16.3	-4.2 ± 16.6
		10	-0.1 ± 18.3	-0.9 ± 20.2	-4.5 ± 18.9	-5.3 ± 18.1	-5.1 ± 18.0
		15	-3.3 ± 18.7	-4.1 ± 19.7	-7.5 ± 18.8	-8.2 ± 18.3	-8.0 ± 18.4
		20	-6.9 ± 19.9	-6.9 ± 20.5	-8.9 ± 19.6	-9.3 ± 18.8	-9.0 ± 18.7
Type 2	Mean ± SD (%)	5	-0.8 ± 8.5	1.7 ± 15.2	-1.6 ± 17.2	-5.1 ± 14.8	-4.4 ± 15.7
		10	-3.2 ± 11.8	-0.3 ± 19.1	-3.5 ± 21.6	-6.7 ± 16.6	-5.1 ± 16.6
		15	-7.6 ± 15.3	-2.7 ± 21.6	-3.8 ± 25.5	-7.6 ± 19.0	-6.3 ± 17.3
		20	-10.3 ± 19.6	-5.5 ± 24.0	-6.3 ± 26.7	-10.0 ± 20.1	-8.5 ± 17.9
Type 3	Mean ± SD (%)	5	-12.7 ± 32.0	-10.0 ± 23.2	3.0 ± 15.3	4.4 ± 29.5	-1.1 ± 31.7
		10	-16.2 ± 41.9	-15.2 ± 30.4	3.5 ± 21.8	6.8 ± 36.5	-1.9 ± 33.3
		15	-24.9 ± 48.3	-23.5 ± 36.0	6.1 ± 29.2	14.0 ± 43.9	-0.8 ± 36.8
		20	-25.8 ± 53.1	-24.9 ± 38.8	6.0 ± 36.6	12.7 ± 45.4	-1.8 ± 37.0

864